Reynolds number sensitivities in wall-modeled large-eddy simulation of a high-lift aircraft

By R. Agrawal, M. P. Whitmore, K. A. Goc†, S. T. Bose‡ AND P. Moin

1. Motivation and objectives

One of the goals of Certification by Analysis (CbA) is to achieve accurate prediction of aircraft performance at the edges of the flight envelope, specifically in high-lift and post-stall conditions, to minimize the need for costly flight testing (Mauery *et al.* 2021). The industry accuracy requirement for the prediction of maximum lift within these flow regimes is documented to be three lift counts ($\Delta C_L = \pm 0.03$) (Clark *et al.* 2020). Additionally, other quantities of interest include the accurate prediction of the pitching moment and drag for the correct surface pressure distributions. Indirectly, this accuracy requirement poses more specific requirements on the details of key flow features, such as the location of transition, mean-three-dimensional juncture flow effects (Lee & Pulliam 2019; Lozano-Durán *et al.* 2020*a*), and smooth-body separations (Rumsey *et al.* 2019). Accurately predicting these flow phenomena using a unified framework is necessary for making significant strides toward CbA.

Conventional computational methods involve the Reynolds-averaged Navier-Stokes equations framework (RANS), in which the mean flow equations are solved and the entirety of the turbulence is modeled. The Fourth AIAA High-Lift Prediction Workshop has shown that existing RANS methods may provide inaccurate solutions near and post aerodynamic stall when the flow experiences large separation bubbles and strong unsteady effects (Ciloni *et al.* 2022; Park *et al.* 2023; Ashton *et al.* 2022). Moreover, the widespread differences in the predictions of lift between the different RANS models and codes have also indicated the shortcomings of the methodology. Instead, recently, large-eddy simulation (LES) methodology has emerged as a supporting technology capable of providing high-fidelity predictions of realistic aircraft geometries in high-lift conditions at affordable cost (Goc *et al.* 2021; Kiris *et al.* 2023). The premise of wall-modeled large-eddy simulation (WMLES) is based on resolving the large-scale flow features on the computational grid. Unlike in RANS, in large-eddy simulation, only the small-scale features are modeled. These small-scale features are often assumed to be universal across flows and governed by the turbulent energy cascade (i.e. the transfer of energy from larger scales to smaller scales). The most commonly used approach for this purpose is the introduction of an eddy viscosity in the simulations that accounts for the unresolved turbulence. For homogeneous flows, it can be shown (Meneveau *et al.* 1992) that the role of the subgrid-scale model is primarily to dissipate energy to maintain the proper spectral characteristics of the energy flux. However, for anisotropic flows, the subgrid-scale model may play an additional role in contributing differently to the different Reynolds stress components. Specifically, for wall-bounded flows, as the Reynolds number increases, the smallest-length scales near the wall become smaller, relative to the largest scales, thereby increasing the computational cost of resolving all or even most of the turbulence (Choi &

† The Boeing Company
‡ Cadence Design Systems & ICME, Stanford University

Moin 2012). In these scenarios, a wall model is employed to provide a modeled boundary condition to the discretized governing equations (e.g. a wall shear stress or a heat flux). Generally, wall models are inspired by the RANS framework in that the mean governing equations are solved from the wall up to the matching location, the location where the wall model exchanges information with the outer LES solution (Bose & Park 2018). For complex flows such as the flow over an aircraft, the near-wall turbulence may not be in dynamical equilibrium and the boundary layer history effects may become important (Bobke *et al.* 2017). Regardless, in most practical WMLES calculations of external aerodynamic flows, these effects are not explicitly included in the wall model. Despite this, WMLES has been successful in predicting some of these complex flow phenomena, such as the accurate prediction of the juncture flow (Lozano-Durán *et al.* 2020*b*, 2022), pressure-gradient-driven smooth-body separation (Agrawal *et al.* 2022*a*,*b*; Whitmore *et al.* 2021), and transonic flow separation (Goc *et al.* 2023; Agrawal *et al.* 2023).

While the aforementioned studies have been largely successful, the effect of the Reynolds number on the predictive capabilities of wall-modeled LES for external aerodynamics has not been thoroughly tested. For instance, for most of the flows mentioned above, the Reynolds number (based on a large-scale geometric length scale and the freestream velocity) is between 1×10^6 and 5×10^6; however, for realistic flight, the Reynolds numbers are an order of magnitude larger. This brief aims to examine the Reynolds number sensitivities of the integrated forces and moments. This computational study is performed as a blind test, i.e., without knowledge of experimental results for the aircraft model for comparison. Despite the present unavailability of experimental data for validation, this article benefits from the knowledge and practices from prior research at the Center for Turbulence Research at Stanford University (Lehmkuhl *et al.* 2018; Goc *et al.* 2021; Lozano-Durán *et al.* 2022), where WMLES was used to simulate realistic aircraft configurations. This work is an important extension of the previous studies to establish the robustness of the methodology to large changes in Reynolds number, which may impose stricter grid resolution requirements and pose a greater predictive challenge to LES models.

In this work, we utilize the charLES flow solver (Brès *et al.* 2018) for performing WMLES. This solver provides a framework consisting of a combination of physics-based modeling choices and low-dissipation numerical methods. The article is organized as follows. In Section 2, we describe the governing equations being solved, and the formulation of the subgrid-scale and wall models employed in this work. In Section 3, we describe the charLES solver and the setup (including the boundary conditions) of the free air simulations. Section 4 discusses the results across several angles of attack and Reynolds number sweeps. Section 5 discusses the effect of the subgrid-scale model on the aforementioned predictions. Finally, some conclusions are drawn in Section 6.

2. Governing equations and modeling approaches

The coarse-grained, or filtered, large-scale fields in a large-eddy simulation are defined by applying a low-pass filter to the transported variables. If the grid-filter kernel is denoted as $\mathcal{G}$, then the filtered field, $\overline{f}$, is given as

$$\overline{f}(x) = \int \mathcal{G}(x, x') f(x') dx', \tag{2.1}$$

with the integral extending over the simulation domain. For compressible flows, it is convenient to define the Favre average, $\tilde{f}$, where

$$\tilde{f} \equiv \frac{\overline{f\rho}}{\overline{\rho}}. \tag{2.2}$$

The governing equations for LES are formally derived by applying the aforementioned grid-filter kernel to the Navier-Stokes equations. The resulting equations for a compressible, nonreacting turbulent flow are given as

$$\frac{\partial \overline{\rho}}{\partial t} + \frac{\partial(\overline{\rho}\ \tilde{u}_i)}{\partial x_i} = 0, \tag{2.3}$$

$$\frac{\partial(\overline{\rho}\ \tilde{u}_i)}{\partial t} + \frac{\partial(\overline{\rho}\ \tilde{u}_j\ \tilde{u}_i)}{\partial x_j} = -\frac{\partial \overline{p}}{\partial x_i} + \frac{\partial(\mu \tilde{S}^d_{ij})}{\partial x_j} - \frac{\partial \tau^{sgs}_{ij}}{\partial x_j}, \tag{2.4}$$

$$\frac{\partial \overline{E}}{\partial t} + \frac{\partial(\overline{E}\ \tilde{u}_j)}{\partial x_j} = -\frac{\partial(\overline{p}\ \tilde{u}_i)}{\partial x_i} + \frac{\partial(\mu \tilde{S}^d_{ij}\tilde{u}_i)}{\partial x_j} - \frac{\partial(\tau^{sgs}_{ij}\tilde{u}_i)}{\partial x_j} - \frac{\partial Q^{sgs}_j}{\partial x_j} + \frac{\partial}{\partial x_j}\left(\kappa \frac{\partial \overline{T}}{\partial x_j}\right), \tag{2.5}$$

with internal energy, e, density, ρ, temperature, T, viscosity, $\mu(T)$, thermal conductivity, $\kappa(T)$, and velocity vector, $\vec{u} = \{u_1, u_2, u_3\}$. Additionally, $\overline{E} = \overline{\rho}\,\overline{e} + 0.5\overline{\rho}\ \tilde{u}_i\ \tilde{u}_i$ is the sum of the resolved internal and kinetic energies, and $\tilde{S}^d_{ij}$ is the deviatoric part of the resolved strain-rate tensor. The relationship between the temperature and the molecular viscosity is assumed to follow a power law with an exponent of 0.75. A constant molecular Prandtl number approximation, $Pr = 0.7$, allows computation of the thermal conductivity. Two additional terms, τ^{sgs}_{ij} and Q^{sgs}_j, require closure modeling. The subgrid stress tensor, τ^{sgs}_{ij}, is defined as $\tau^{sgs}_{ij} = \overline{\rho}(\widetilde{u_i u_j} - \tilde{u}_j\tilde{u}_i)$. Similarly, $Q^{sgs}_j = \overline{\rho}(\widetilde{eu_j} - \tilde{e}\tilde{u}_j)$ is the subgrid heat flux. In this work, the isotropic component of the subgrid stress is absorbed into the pressure, leading to a pseudo-pressure field. The next subsection describes the closure models employed in this work for τ_{ij}. Note that the subgrid heat flux is modeled using a constant turbulent Prandtl number approximation, $Pr_t = 0.9$, applied with respect to the dissipative component of the subgrid-stress tensor.

2.1. *Subgrid-scale model*

Recent investigations (Agrawal *et al.* 2022*b*; Goc 2023) suggest that dynamic subgrid-scale models provide improved accuracy over constant coefficient models tuned for canonical flows. Informed by these investigations on flows similar to the present aircraft, two dynamic coefficient subgrid-scale models are employed in this work: the dynamic Smagorinsky model (DSM) of Moin *et al.* (1991), and the recently proposed dynamic tensorial coefficient Smagorinsky model (DTCSM) of Agrawal *et al.* (2022*b*). The specific mathematical formulations of these models are excluded here for brevity. The performance of these models has been extensively verified and validated in our computational solver in previous studies (Goc *et al.* 2021, 2023; Agrawal *et al.* 2022*a*, 2023).

2.2. *Wall model*

In this work, an algebraic form of the equilibrium wall-stress model (EQWM) is used in which the assumed mean velocity profile is a C^1 continuous piecewise fit of the viscous sublayer and the logarithmic layer. This model has been shown to have the same predictive capabilities as the ordinary-differential-equation-based counterpart in flows without significant compressibility effects, while allowing a reduced computational cost (Goc 2023). Details of the compressible formulation of the EQWM can be found in

(Lehmkuhl *et al.* 2018). Unlike some of the previously reported studies that use higher off-wall matching points to avoid numerical inaccuracies (Kawai & Larsson 2012), first-point matching is used in the present study. Prior work by the authors with this solver and meshing strategy (Voronoi-diagram-based meshes seeded from hexagonally close-packed points) has not shown evidence of a log-layer mismatch when using a first-point matching location in the simulation of a turbulent channel flow at $Re_\tau = 4200$ with a nominal resolution of 20 uniformly distributed cells in the channel half-height.

3. Solver details and computational setup

The simulations presented in this work are performed using charLES, an explicit, unstructured, finite-volume solver for the compressible Navier-Stokes equations. This code is formally second-order accurate in space and third-order accurate in time, and utilizes Voronoi-diagram-based grids. More details of the solver as well as validation cases can be found in Brès *et al.* (2018) and Goc *et al.* (2021). The solver uses operators that are formally skew-symmetric to conserve kinetic energy in the current simulations. The numerical discretization in the code also approximately preserves entropy.

The geometry simulated is the NASA Common Research Model High-Lift aircraft, which is the focus of the Fifth High-Lift Prediction Workshop (as a part of the AIAA Aviation Forum meeting, 2024). The current simulations do not include the complex effects of the National Transonic Facility (NTF) wind tunnel, as limited information is available about the mass bleed capabilities and boundary layer growth on the tunnel walls. The simulation geometry is maintained to be similar to the test article, including the bracketry associated with deployed high-lift devices (flaps/slats) and an open nacelle mounted on the underside of the wing. The reference Reynolds number, Re_{MAC}, is defined based on the freestream velocity and the mean aerodynamic chord (MAC). In this study, three Reynolds numbers are considered: 5.5, 16 and 30 million. The freestream Mach number is subsonic at $M = 0.2$.

The half-span geometry is placed inside a hemispherical domain with a radius of $1000 \times MAC$, where freestream conditions are imposed. The boundary conditions in the simulations closely follow the efforts of Goc *et al.* (2023*b*). At the hemispherical inlet, a uniform plug flow (in the cardinal and not the radial direction) is fed. All solid boundaries on the aircraft model are treated viscously with the algebraic equilibrium wall model. As the nominal Reynolds number increases, the boundary layer on the wing is expected to trip earlier along the streamwise direction, thereby making the application of the turbulent wall model more appropriate. For flows with significant pressure gradients such as the ones studied in this work, the equilibrium assumption of near-wall eddies may be challenged; however, for this blind study, the equilibrium wall model is invoked. At the aft part of the hemisphere, a characteristic nonreflecting boundary condition is specified with an outlet pressure (Poinsot & Lele 1992). The symmetry plane is treated with a stress-free boundary condition. For simulations including the full span of the aircraft, the aircraft geometry is mirrored across this plane.

Slices of the grid are shown in Figure 1. The grids are generated by computing a Voronoi diagram of the watertight volume around the aircraft, using a hexagonal close-packed (HCP) point seeding, which is then smoothed via Lloyd iterations to be made more centroidal, as done by Du *et al.* (2006), and results in the grid topology shown in the figure. The cells are locally isotropic, and refinement windows are set according to the distance to the nearest boundary. This gridding approach is low-touch, in the sense

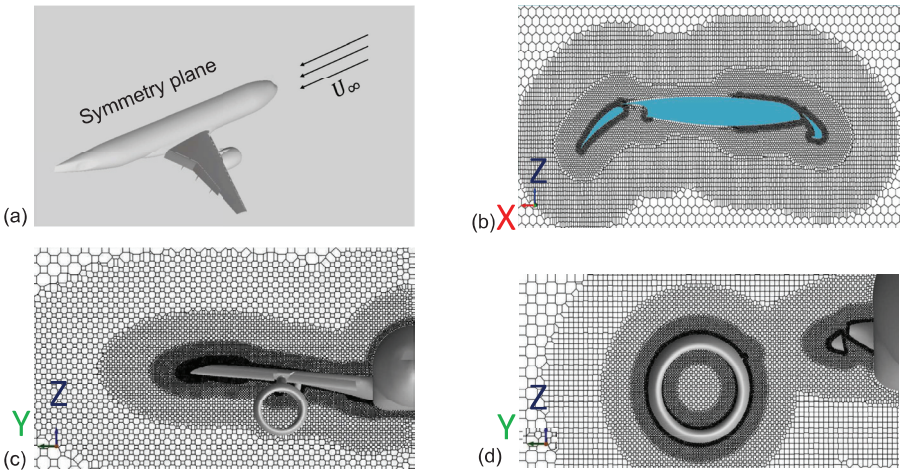

FIGURE 1. A representation of (a) the computational domain for simulating the NTF CRM High Lift geometry and (b) the grid distribution on the three-element airfoil slice (taken at mid-span of the main wing element). (c) and (d) are frontal views of the aircraft model showing the grid distribution around the fuselage and the nacelle, respectively. Note that these images represent a "very, very coarse" grid (4× coarser in physical dimensions in all directions than the coarsest grid simulated).

that no particular attention is paid to resolving specific flow features, to fairly evaluate the predictive capabilities of WMLES methodology. A grid-refinement iteration involves refining the near-wall cell layers by a factor of two while keeping the overall background resolution constant. For example, a 384 million control volume (Mcv) grid is obtained by inserting a five-cell-thick layer of twofold refined isotropic, HCP cells (onto an existing 102 Mcv grid) next to the solid walls. Table 1 provides more detailed information about the minimum cell resolution and approximate points per boundary layer thickness (per a zero-pressure-gradient boundary layer estimate) for the present simulations.

Figure 2 shows the achieved resolution on the medium grid by plotting y^+, which is the half-height of the first computational grid cell, scaled in viscous inner units. Note that the y^+ contours in this figure correspond to the location where the wall model and the outer LES solution exchange information to provide the wall shear stress and the heat flux. A wide range of the y^+ is visible, highlighting that the wall models need to account for multiple Reynolds number and pressure-gradient effects. At $\alpha = 7.05°$, the darker blue contour regions indicate the small pockets of separated flow on the trailing flap. Similarly, for $\alpha = 19.57°$, the outboard wing also shows an indication of separation bubbles on the main element. It is expected that for $Re_{MAC} = \{16, 30\} \times 10^6$, the values of y^+ increase since the physical dimensions of the grids are maintained to be the same. From rudimentary flat plate zero-pressure-gradient boundary layer estimates, this change would scale approximately as $Re^{13/14}$, thus making the y^+ for $Re_{MAC} = \{16, 30\} \times 10^6$ cases approximately $\{2.7, 4.8\}\times$, respectively, the y^+ value of the $Re_{MAC} = 5.5 \times 10^6$ case. In viscous units, the first cell resolution lies between $y^+ \in [0, 150]$ on the medium grid, which demonstrates the large changes in the near-wall flow structure. Some key flow phenomena that are responsible for these variations include large favorable/adverse pressure gradients and flow separation. The sharp changes in the value of y^+ visible in

Grid	Points per MAC	Total CVs (millions)	Min. resolution (mm)	$\frac{\delta_{zpg}}{\Delta}$
Coarse	1024	102	6.8	~ 10
Medium	2048	384	3.4	~ 20
Fine	4096	1500	1.7	~ 40

TABLE 1. The variation in the number of points per mean aerodynamic chord (MAC), the total number of control volumes (CVs), the minimum resolution, and an estimate of the number of points in the equivalent zero-pressure-gradient boundary layer at the trailing edge of the wing (around midspan) for $Re_{MAC} = 30 \times 10^6$.

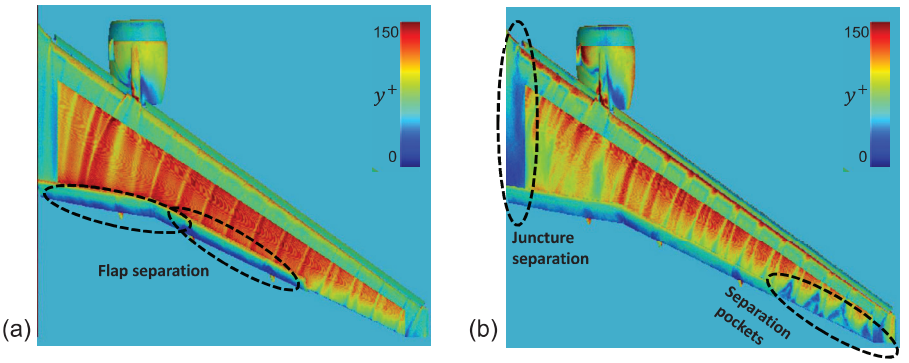

FIGURE 2. The contour of average y^+ at (a) $\alpha = 7.05^\circ$ and (b) $\alpha = 19.57^\circ$ for the medium grid employed in the current simulations for the high-lift aircraft model at $Re_{MAC} = 5.5 \times 10^6$. Note that the small y^+ near the inboard wing at $\alpha = 19.57^\circ$ is because of the large inboard separation.

Figure 2 reflect changes to the local grid spacing associated with targeted refinement regions at the leading edges of the wing/nacelle and at the wing root/tip following the work of Goc (2023); Goc *et al.* (2023*b*) and Lozano-Durán *et al.* (2020*a*).

The angles of attack, α, simulated for the $Re_{MAC} = 5.5 \times 10^6$ and $Re_{MAC} = 16 \times 10^6$ cases are $\alpha \in \{2.78, 7.05, 11.29, 17.05, 19.57, 20.46, 21.57\}^\circ$, and those for the $Re_{MAC} = 30 \times 10^6$ case are $\alpha \in \{6, 10, 14, 16, 18, 19, 20, 21, 22\}^\circ$. The angles of attack for the lower Reynolds numbers were chosen to match the test-case angles from the Fourth AIAA High-Lift Prediction Workshop. The angles of attack for the highest Reynolds number case are chosen to cover a comprehensive range of the lift curve, including low-angle, maximum lift, stall, and post-stall regimes; at the time of this work, the angles for the relevant test case of the Fifth High-Lift Prediction Workshop were not released.

4. Results for the free air configuration

4.1. *Grid-refinement sweep for* $Re_{MAC} = 5.5 \times 10^6$

By performing a grid-refinement sweep for the NTF Geometry at $Re_{MAC} = 5.5 \times 10^6$, a comparison between the NTF and the QinetiQ high-lift aircraft models can be made. For this purpose, free air simulations of the NTF geometry are compared to the experimental data of Evans *et al.* (2020), corrected for wind-tunnel effects. There are several differences between the two geometries, the first being the positioning of the flaps. The QinetiQ

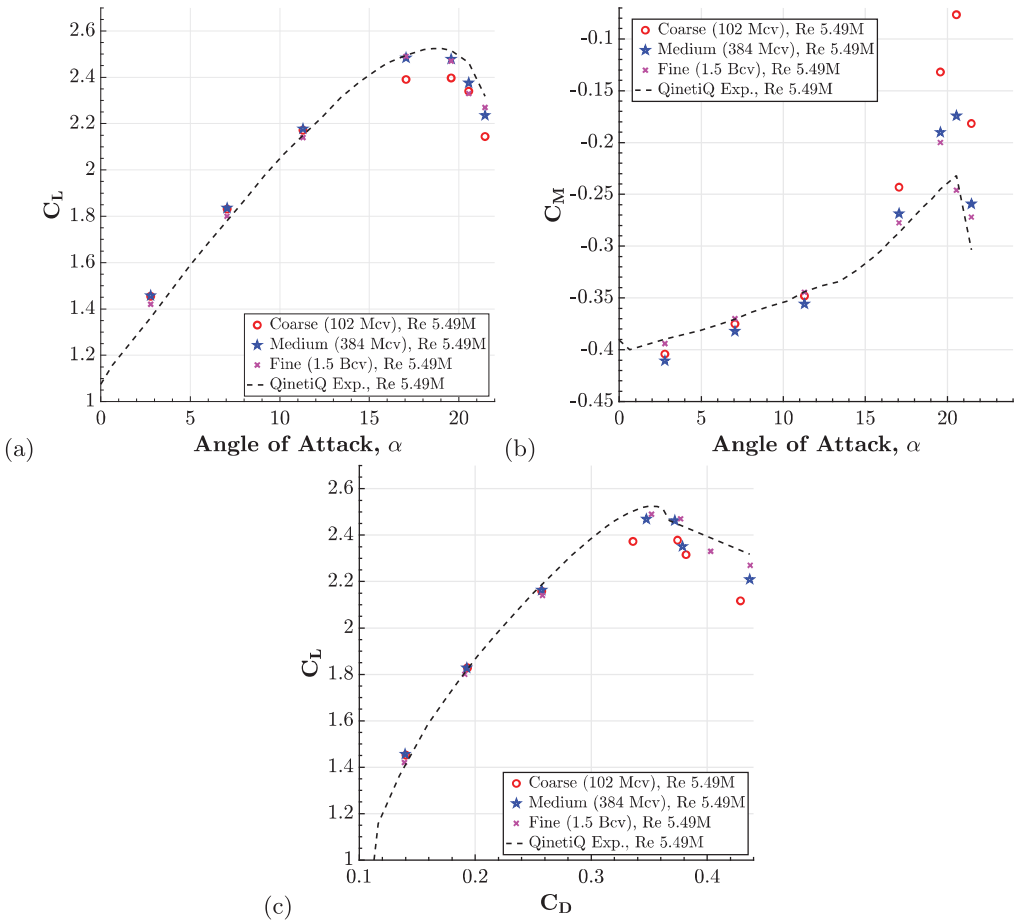

FIGURE 3. The grid-resolution sensitivity of integrated quantities such as (a) C_L, (b) C_M and (c) $C_L - C_D$ across an angle-of-attack sweep for $Re_{MAC} = 5.5 \times 10^6$ aircraft model. The experimental data from the QinetiQ facility (Evans *et al.* 2020) are included for qualitative comparison, as the aircraft geometry in that experiment differed slightly from the present geometry, and, thus, the WMLES is not expected to match.

geometry has the inboard flap positioned higher than the NTF geometry, and vice versa for the outboard flap. Additionally, there are some differences in the positioning of the bracketry, and some differences in the slat and nacelle-lip contouring that may affect the stall characteristics of the aircraft model. Because of these differences, exact agreement between these experimental data and the present simulations is not expected.

Figure 3 provides the grid-refinement sweep of the integrated quantities, C_L, C_M and C_D, over the aircraft model. At low angles of attack, the differences between WMLES and prior experiments are small and diminish on grid refinement. Similar to the previous observations of Goc *et al.* (2021); Goc *et al.* (2023*b*), some nonmonotonic convergence of the simulations toward the reference experiments is observed. However, the differences between the solutions on the three grids here are considerably weaker. However, on the larger angles, especially near stall, the differences in C_M are most clearly visible. For this configuration, the aircraft stall occurs at a similar angle to the QinetiQ geometry;

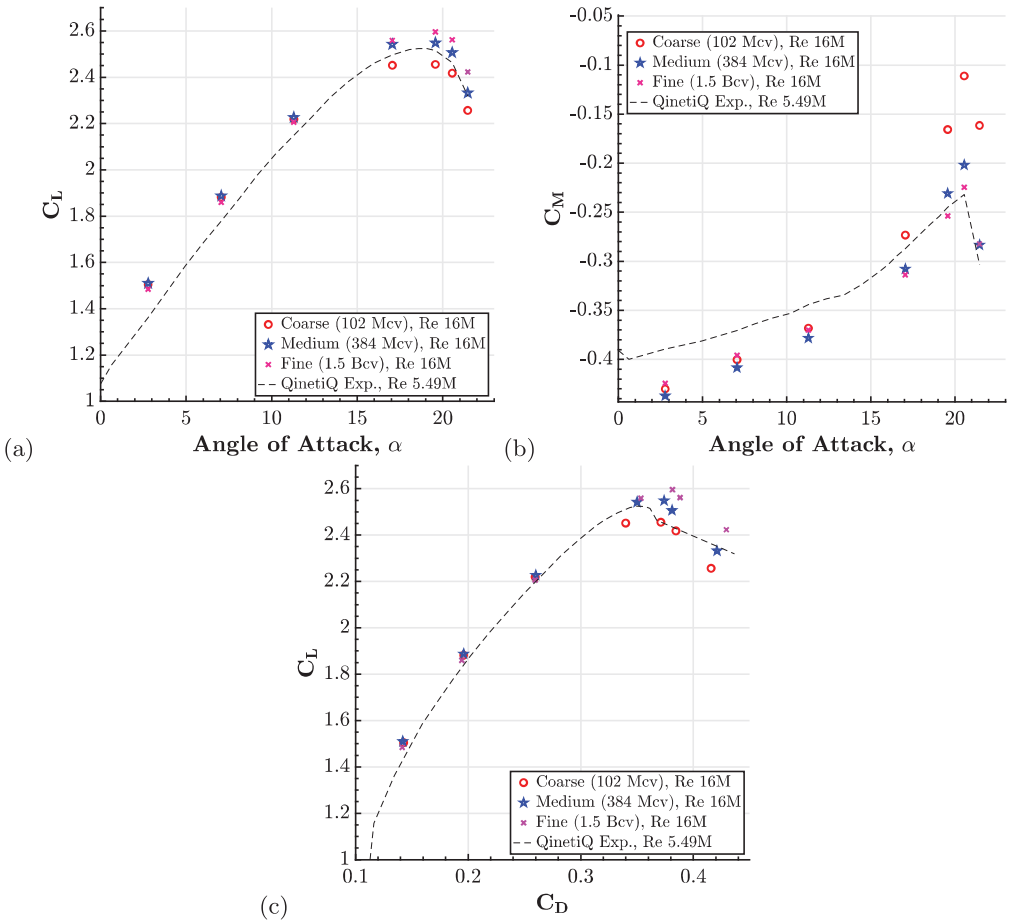

FIGURE 4. The grid-resolution sensitivity of integrated quantities such as (a) C_L, (b) C_M and (c) $C_L - C_D$ across an angle of attack sweep for $Re_{MAC} = 16 \times 10^6$ aircraft model. The experimental data from the QinetiQ facility (Evans *et al.* 2020) are included only to orient the reader, as the geometry and Reynolds number differ, and, thus, the WMLES is not expected to match.

however, the break in the pitching moment is observed earlier for the NTF geometry. For a similar maximum lift at $\alpha \sim 19°$, the pitching moment for the NTF geometry is much less negative than the QinetiQ experiments, which suggests a larger part of the lift is distributed in the inboard regions of the aircraft on the NTF geometry. At the stall condition, $\alpha = 20.57°$, the NTF moment is more pitch-down than the QinetiQ experiments, making the stall shallower. Post-stall, at $\alpha = 21.46°$, the moment is more pitch-down, thus making the width of the shallow stall smaller. The drag characteristics of the NTF model are similar to those of QinetiQ for the lower angles of attack. At the higher angles, the $C_L - C_D$ profile shifts slightly forward (higher drag for the same lift) for the NTF geometry compared to the QinetiQ experiments. Especially at the stall angle, the drag value for the NTF model is much higher than the QinetiQ model.

4.2. *Grid-refinement sweep for* $Re_{MAC} = 16 \times 10^6$

The sensitivity of the lift, pitching moment and drag to the Reynolds numbers are studied by increasing the Reynolds number to $Re_{MAC} = 16 \times 10^6$. Figure 4 presents these quantities. As expected, the increased Reynolds number results in an increased lift across the angle-of-attack sweep. Since the flap separation at low angles of attack is essentially a low–Reynolds number phenomenon (Kiris *et al.* 2023), it is expected that the separation will be diminished at $Re_{MAC} = 16 \times 10^6$. Since the integrated lift and moments are primarily due to the pressure differences on the aerodynamic surfaces as the flow becomes more attached, the grid requirements to predict the correct lift and moment are driven from the inviscid pressure gradient and not from the viscous flow resolution. It is also observed for the three lowest angles of attack, $\alpha = 2.78°,\ 7.05°,\ 11.29°,\ 17.05°$, that the grid sensitivities in the solutions are small and the results are reasonably converged. For the higher angles of attack, in pre-stall conditions, the leading edge acceleration of the flow becomes increasingly important. It is hypothesized that, as the grid is refined, this acceleration can be better captured, and, consequently, the lift and drag increase. Between the coarse and medium, and the medium and fine grids, the ΔC_L changed from $\Delta C_L = 0.10$ to $\Delta C_L = 0.05$. Simulations using a grid with further refinement (approximately 6 billion control volumes) are currently being pursued, and it is anticipated that the differential lift will drop below $|\Delta C_L| < 0.03$, which was suggested as a reasonable simulation accuracy criterion by Clark *et al.* (2020). Although not shown here, numerical experiments on a multi-element two-dimensional airfoil configuration (Chin *et al.* 1993) have suggested that the grid resolution requirement to accurately capture the peak C_L scales as $Re^{1/7}$ with the chord Reynolds number.

4.3. *Grid-refinement sweep for* $Re_{MAC} = 30 \times 10^6$

The highest Reynolds number considered in this work, $Re_{MAC} = 30 \times 10^6$, approaches the order of a realistic flight Reynolds number, $Re_{MAC} \sim O(50 \times 10^6)$. For this flow, the lift is expected to increase compared to the $Re_{MAC} = 16 \times 10^6$ flow and the fuselage vortex is expected to become stronger at higher angles of attack. Since the corresponding experimental configuration for this flow is a half-span wall-mounted configuration instead of a full-span sting-mounted configuration, the effect of the symmetry plane may also be an important point of analysis.

Comparing the results in Figure 5 to the previous results in Figures 3 and 4, the lift overall is increased relative to the two lower Reynolds number cases. The lift, moment and drag appear reasonably grid-converged for the lowest angles of attack ($\alpha \lesssim 12°$). At the higher angles, near $C_{L,max}$ and post-stall, large differences between the coarse and the medium grids are observed. At the maximum lift, the fine grid result is still varying compared to the coarse and medium grids. Note that, similar to the $Re_{MAC} = 16 \times 10^6$ case, between the coarse and medium, and the medium and fine grids, the ΔC_L changes from $\Delta C_L = 0.11$ to $\Delta C_L = 0.05$. Therefore, one additional grid refinement will likely lead to an approximately converged result, i.e. within a $\Delta C_L < 0.03$. A very fine mesh with O(6) billion control volumes is currently being pursued. For the medium grid, the post-stall behavior is observed to be different than the lower Reynolds numbers. Specifically, at $\alpha = 22°$, the pitching moment becomes less nose-down for a lower lift and drag than at $\alpha = 21°$; however, it is difficult to make a conclusive comparison as the angles of attack differ and the change in the moment with respect to the angle of attack is expected to be sharp around the pitch break.

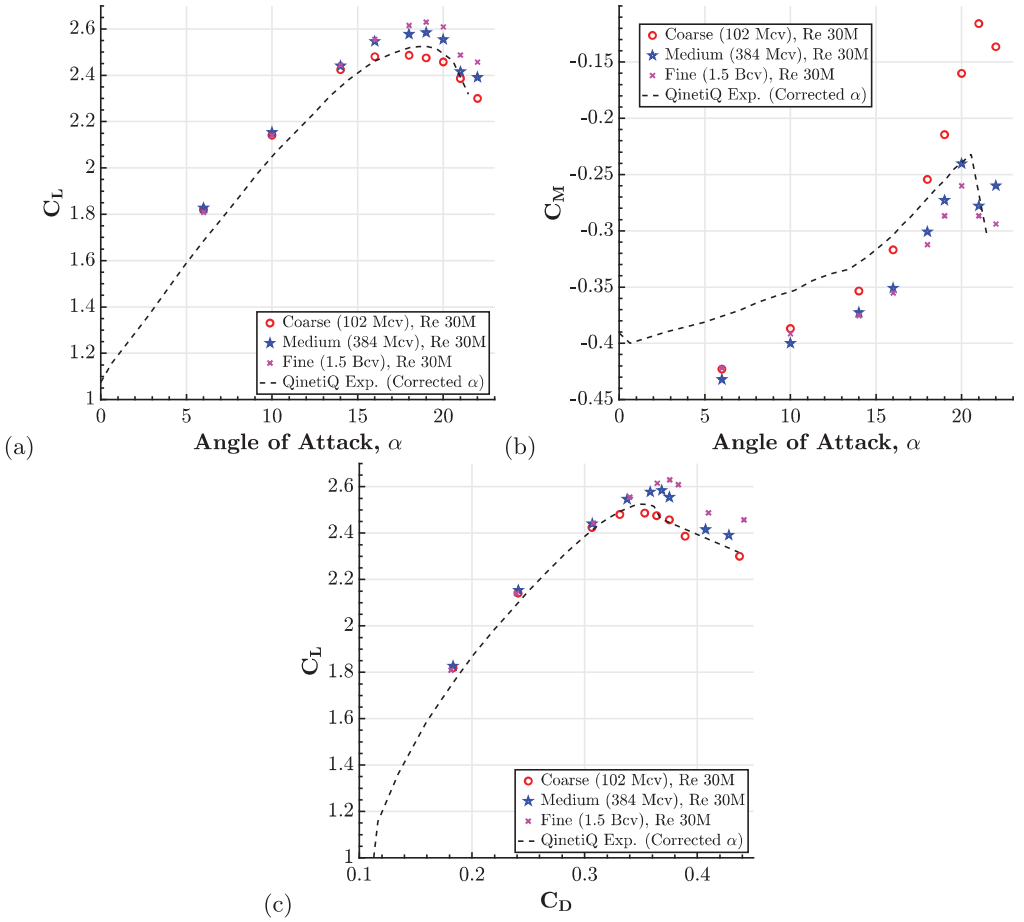

FIGURE 5. The grid-resolution sensitivity of integrated quantities such as (a) C_L, (b) C_M and (c) $C_L - C_D$ across an angle-of-attack sweep for $Re_{MAC} = 30 \times 10^6$ aircraft model. The experimental data from the QinetiQ facility (Evans *et al.* 2020) are included only to orient the reader, as the geometry and Reynolds number differ, and, thus, the WMLES is not expected to match.

4.4. *Effect of the symmetry plane*

Fundamentally, the applied boundary condition on the symmetry plane is a stress-free condition with no instantaneous penetration. In a Reynolds-averaged framework, this is the correct boundary condition at the symmetry plane since there is no mean flow that crosses the symmetry plane; however, in LES, there exist finite turbulence fluctuations normal to the symmetry plane. Hence, a boundary condition that instantaneously imposes no transpiration is ill-motivated. The strength of these fluctuations is expected to increase at higher Reynolds numbers, especially at higher angles of attack when the unsteadiness of the fuselage vortex may become important. To test this hypothesis, a full-span simulation is performed by mirroring the aircraft geometry about the symmetry plane.

The results in Figure 6 suggest that, on the medium grid, the integrated quantities remain largely unaffected for all angles of attack. In the post-stall regime, at $\alpha = 21°$, a minor discrepancy between the half and the full-span configuration results is observed.

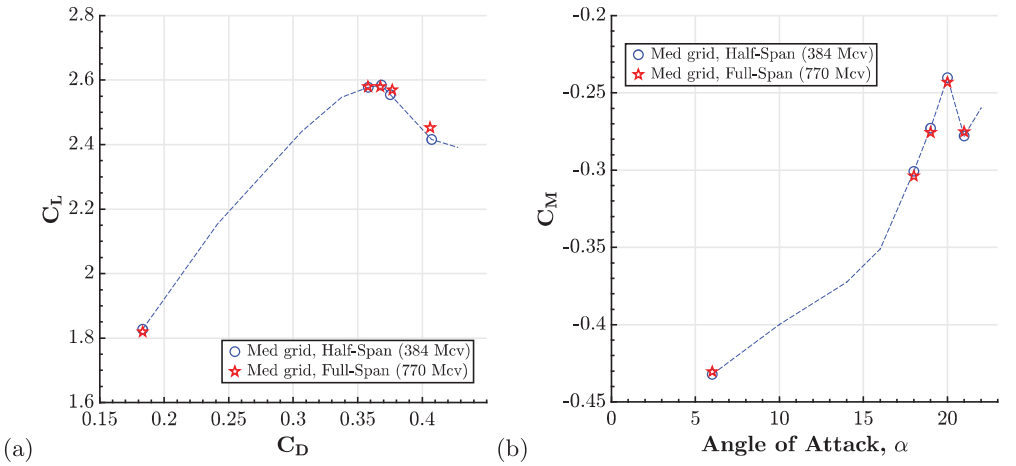

FIGURE 6. The effect of the symmetry plane on the integrated quantities, (a) $C_L - C_D$ polar and (b) C_M, for $\alpha \in \{6, 18, 19, 20, 21\}^\circ$ for the $Re_{MAC} = 30 \times 10^6$ case. These angles are chosen to highlight the low-angle and stalled flow regimes. The dash-dotted blue lines trace through the predictions on the medium grid in half-span configuration across all the angles-of-attack considered for $Re_{MAC} = 30 \times 10^6$ flow.

Additionally, the stall angle is insensitive to the symmetry plane. These results suggest that the presence of normal turbulent fluctuations at the center plane does not contribute significantly to the strength of the fuselage vortex in a way that affects the integrated forces and moments.

5. Sensitivity to the subgrid-scale model

In this section, a brief comparison between the performance of the two dynamic subgrid-scale models is considered. Since the effect of the subgrid-scale model is likely to be the largest on coarse grids at higher Reynolds numbers, we perform a comparative study at $Re_{MAC} = 30 \times 10^6$ for the coarse and medium grids for selected angles, $\alpha \in \{6, 14, 18, 19, 20, 21, 22\}^\circ$. Additionally, one angle, $\alpha = 19^\circ$, is considered on the fine grid.

Figure 7 provides a comparison in the integrated quantities between DSM and DTCSM subgrid-scale models. On both the coarse and medium grids, the two models provide similar answers for the lower angles of attack. However, in the near and post-stall regions, for $\alpha = 18^\circ - 22^\circ$, the differences on the coarse grid are larger. The tensorial subgrid-scale model simulations predict a larger lift and drag with an identifiable pitch break, unlike the standard eddy-viscosity model. Upon grid refinement, for the medium grid, some differences around the stall region remain, with DTCSM results still predicting a slightly higher maximum lift. A clear pitch break is observed for both models on the medium grid. Note also that the higher maximum lift predicted by DTCSM is closer to both the fine-grid DSM and DTCSM results, thereby suggesting that the medium-grid DTCSM result is more accurate than the corresponding DSM result. On the fine grid, both models predict nearly the same values of the integrated loads. Additionally, the change in the lift coefficient with grid refinement, ΔC_L, with DTCSM is slightly smaller than that with DSM.

To further investigate these differences on the coarse and medium grids, differential

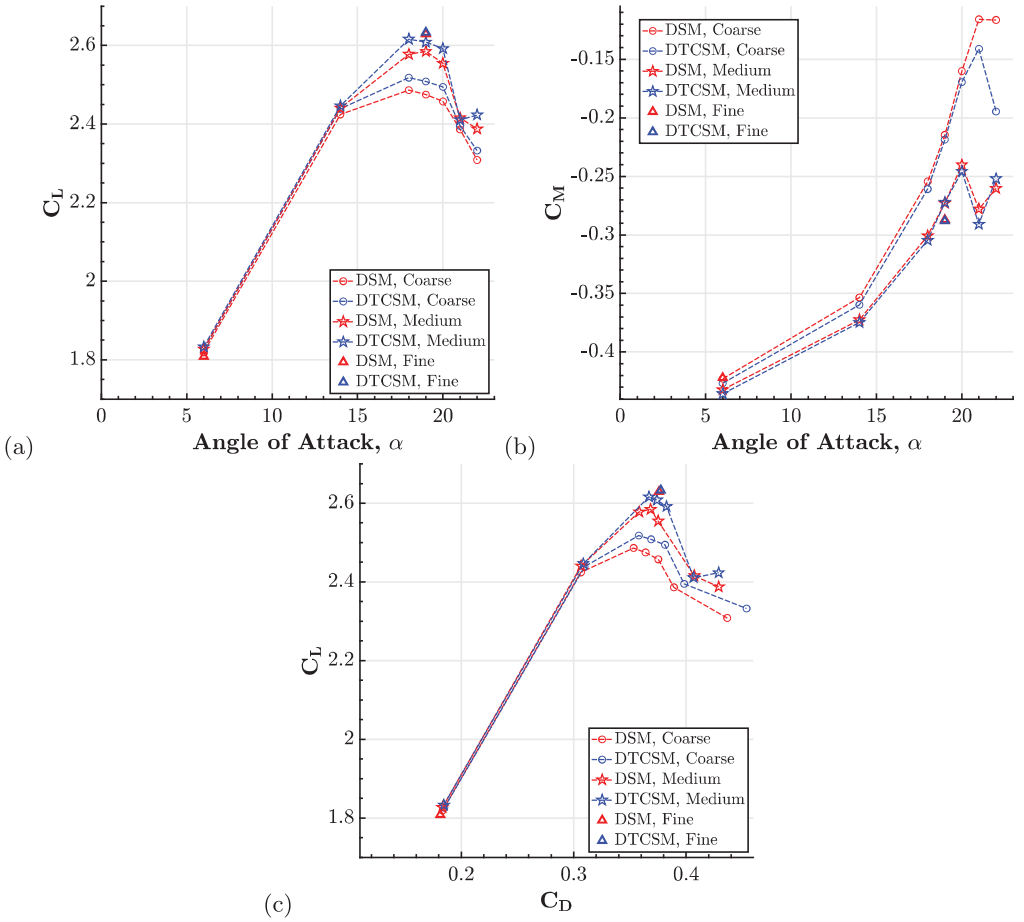

FIGURE 7. A comparison between the predictions of the (a) lift coefficient, C_L, (b) pitching moment coefficient C_M, and (c) lift-drag polar, $C_L - C_D$, between the DSM and DTCSM modeling combinations on the coarse and medium grids for the $Re_{MAC} = 30 \times 10^6$ aircraft model. Note that only selected angles were run with DTCSM for comparison purposes.

surface pressure coefficient contours, denoted as ΔC_p, are shown in Figures 8 and 9 for the $\alpha = 19°$ and $\alpha = 22°$ cases, respectively. This quantity is defined as the difference between two simulations, $\Delta C_p = C_p^{DTCSM} - C_p^{DSM}$, where the individual simulations may be from the same or different grids. Figure 8(a) suggests an increased lift on the medium grid with DTCSM at $\alpha = 19°$ (maximum lift) that comes from increased suction on the inboard flap (the blue regions denote a higher suction in the DTCSM result). In Figure 8(b), the medium-grid DTCSM is compared to the fine-grid DSM result, and the differences on the flap are smaller. Although not shown, it was verified that the C_p distribution on the two fine-grid results from DSM and DTCSM are similar everywhere on the wing. What these results show is that the faster convergence of C_L when using DTCSM is due to the ability of the WMLES to better capture the flow features on a coarser grid, when compared to simulations using DSM.

The differences in the medium-grid DTCSM and fine-grid DSM are predominantly visible in the signatures of the wingtip and the fuselage vortices. For the post-stall regime,

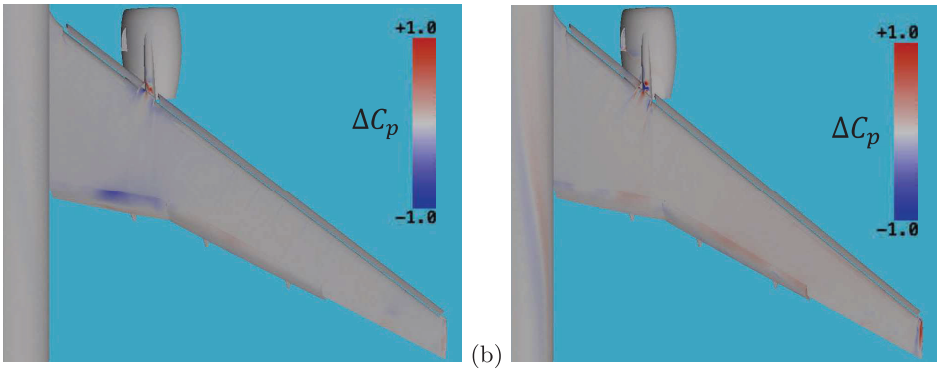

FIGURE 8. Differential values of the local C_p on the suction side of the wing at $\alpha = 19^\circ$ (a) between the DTCSM and DSM results on the medium grid and (b) between DTCSM result on the medium grid and the DSM result on the fine grid. The case shown is at $Re_{MAC} = 30 \times 10^6$. The differential pressure is defined as $\Delta C_p = C_p^{DTCSM} - C_p^{DSM}$. A blue value (negative) in the color contour highlights a region with higher suction in the DTCSM case relative to the DSM case, and vice versa for a red value (positive). The large gray regions indicate little difference in the local pressure values over most of the wing.

$\alpha = 22^\circ$, on the coarse grid, DTCSM produces a larger lift and a stronger nose-down pitching moment than DSM. As shown in Figure 9(a), these differences are primarily due to an increased suction on the outboard slat and main-element sections and decreased suction on the inboard slat, juncture and outboard flap. These locally lower suction forces in the juncture region and the outboard flap region are representative of the separation patterns observed post-stall on a lower Reynolds number aircraft (Evans *et al.* 2020). On the medium grid, in Figure 9(b), the solutions for the two models become more similar. However, DTCSM still predicts a slightly lower suction in part of the juncture region, whereas, aft of the nacelle, the predicted suction from DTCSM is higher. This suggests a slightly smaller spanwise extent of the inboard separation bubble with DTCSM. In the outboard regions, DTCSM predicts slightly higher lift around the leading edges of the slat and the main element, while also predicting slightly more separated flow on the trailing edges.

6. Conclusion

Wall-modeled large-eddy simulations (WMLES) have been performed to assess the Reynolds number sensitivities on the predictions of the lift, pitching moment and drag of a high-lift aircraft model. These simulations have been pursued as a blind study for which experimental results are not yet available for validation. The differences between the presently studied Common Research Model geometry (the focus of the NTF experimental campaign) and the prior QinetiQ experimental geometry are primarily concentrated on the contouring of the nacelle lip and the slat leading edges, as well as the positioning of the flaps. For the same Reynolds number, WMLES predicts higher drag for the NTF aircraft model than that of the QinetiQ experiments near stall. The initial investigations have also suggested an increase in lift across the angle-of-attack sweep as the Reynolds number is increased, with some degree of grid convergence on the low angles of attack. Converging the maximum lift to within $\Delta C_L = 0.03$ is being pursued by further grid refinement. For the $Re = 30 \times 10^6$ case, the impact of the symmetry plane was found

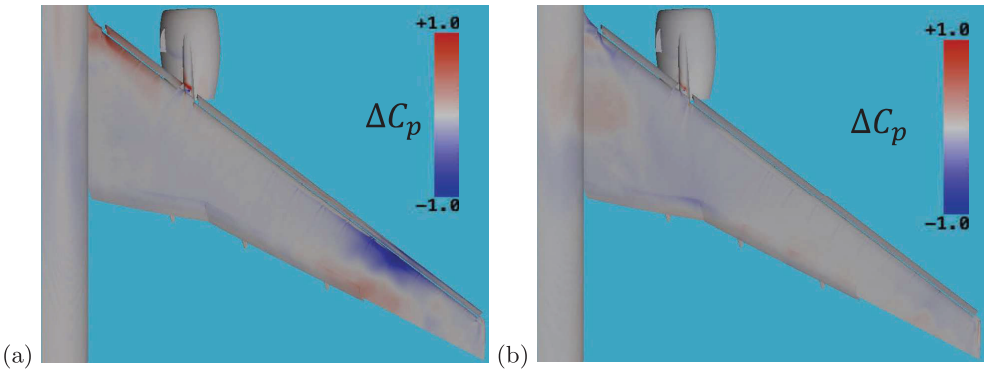

(a) (b)

FIGURE 9. The difference in local C_p on the suction side of the wing at $\alpha = 22^\circ$ (a) between the DTCSM and the DSM results on the coarse grid and (b) between the DTCSM and the DSM results on the medium grid. The case shown is at $Re_{MAC} = 30 \times 10^6$. The differential pressure is defined as $\Delta C_p = C_p^{DTCSM} - C_p^{DSM}$. A blue value (negative) in the color contour highlights a region with higher suction in the DTCSM case relative to the DSM case, and vice versa for a red value (positive). The large gray regions indicate little difference in the local pressure values over most of the wing.

to be minimal. Subgrid-scale modeling sensitivities between the dynamic Smagorinsky model (DSM) and the dynamic tensor coefficient Smagorinsky model (DTCSM) are also noted at this Reynolds number, with DTCSM providing solutions resembling finer grid results from DSM.

Acknowledgments

This work was supported by NASA's Transformational Tools and Technologies project under grant #80NSSC20M0201. This research used resources of the Oak Ridge Leadership Computing Facility, which is a DOE Office of Science User Facility supported under Contract DE-AC05-00OR22725.

REFERENCES

AGRAWAL, R., BOSE, S. T., & MOIN, P. 2022*a* Wall modeled LES of the Boeing speed bump using a non-Boussinesq modeling framework. *Annual Research Briefs*, Center for Turbulence Research, Stanford University, pp. 43–58.

AGRAWAL, R., ELNAHHAS, A., & MOIN, P. 2023 Wall modeled large-eddy simulations of flow over the Sandia transonic hump. *AIAA Paper* # 2023-3971.

AGRAWAL, R., WHITMORE, M. P., GRIFFIN, K. P., BOSE, S. T., & MOIN, P. 2022*b* Non-Boussinesq subgrid-scale model with dynamic tensorial coefficients. *Phys. Rev. Fluids* **7**, 074602.

ASHTON, N., BATTEN, P., CARY, A. W., HOLST, K. R., & SKAPERDAS, V. 2022 HLPW-4/GMGW-3: Hybrid RANS/LES technology focus group workshop summary. *AIAA Paper* # 2022-3293.

BOBKE, A., VINUESA, R., ÖRLÜ, R., & SCHLATTER, P. 2017 History effects and near equilibrium in adverse-pressure-gradient turbulent boundary layers. *J. Fluid Mech.* **820**, 667–692.

BOSE, S. T. & PARK, G. I. 2018 Wall-modeled large-eddy simulation for complex turbulent flows. *Ann. Rev. Fluid Mech.* **50**, 535–561.

Brès, G. A., Bose, S. T., Emory, M., Ham, F. E., Schmidt, O. T., Rigas, G., & Colonius, T. 2018 Large-eddy simulations of a co-annular turbulent jet using a Voronoi-based mesh generation framework. *AIAA Paper* # 2018-3302.

Chin, V., Peters, D., Spaid, F., & McGhee, R. 1993 Flowfield measurements about a multi-element airfoil at high Reynolds numbers. *AIAA Paper* # 1993-3137.

Choi, H. & Moin, P. 2012 Grid-point requirements for large eddy simulation: Chapman's estimates revisited. *Phys. Fluids*, 011702.

Ciloni, P. A., Souza, M. A., Scalabrin, L. C., & Antunes, A. 2022 HLPW4-impact of solution strategy on CFD RANS simulations of high lift configurations. *AIAA Paper* # 2022-3393

Clark, A. M., Slotnick, J. P., Taylor, N. J., & Rumsey, C. L. 2020 Requirements and challenges for CFD validation within the High-Lift Common Research Model ecosystem. *AIAA Paper* # 2020-2772.

Du, Q., Emelianenko, M., & Ju, L. 2006 Convergence of the Lloyd algorithm for computing centroidal Voronoi tessellations. *SIAM J. Numer. Anal.* **44**, 102–119.

Evans, A. N., Lacy, D. S., Smith, I., & Rivers, M. B. 2020 Test summary of the NASA High-Lift Common Research Model half-span at QinetiQ 5-metre pressurized low-speed wind tunnel. *AIAA Paper* # 2020-2770.

Goc, K., Agrawal, R., Moin, P., & Bose, S. 2023*a* Studies of transonic aircraft flows and prediction of initial buffet onset using large-eddy simulations. *AIAA Paper* # 2023-4338.

Goc, K. A. 2023 Towards certification by analysis: Large-eddy simulations of commercial aircraft across the flight envelope. Ph.D. thesis, Stanford University.

Goc, K. A., Lehmkuhl, O., Park, G. I., Bose, S. T., & Moin, P. 2021 Large eddy simulation of aircraft at affordable cost: a milestone in computational fluid dynamics. *Flow* **1**, E14.

Goc, K. A., Moin, P., Bose, S. T. & Clark, A. M. 2023*b* Wind tunnel and grid resolution effects in large-eddy simulations of the high-lift common research model. *J. Aircraft* pp. 1–13.

Kawai, S. & Larsson, J. 2012 Wall-modeling in large eddy simulation: Length scales, grid resolution, and accuracy. *Phys. Fluids*, 015105.

Kiris, C. C., Ghate, A. S., Browne, O. M., Slotnick, J., & Larsson, J. 2023 HLPW-4: Wall-modeled large-eddy simulation and Lattice–Boltzmann technology focus group workshop summary. *J. Aircraft* **60**, 1–23.

Lee, H. C. & Pulliam, T. H. 2019 Overflow juncture flow computations compared with experimental data. *AIAA Paper* # 2019-0080.

Lehmkuhl, O., Park, G. I., Bose, S. T., & Moin, P. 2018 Large-eddy simulation of practical aeronautical flows at stall conditions. *Proceedings of the Summer Program*, Center for Turbulence Research, Stanford University, pp. 87–96.

Lozano-Durán, A., Bose, S. T., & Moin, P. 2020*a* Performance of wall-modeled LES for external aerodynamics in the NASA Juncture Flow. *Annual Research Briefs*, Center for Turbulence Research, Stanford University, pp. 33–48.

Lozano-Durán, A., Bose, S. T., & Moin, P. 2020*b* Prediction of trailing edge separation on the NASA Juncture Flow using wall-modeled LES. *AIAA Paper* # 2020-1776.

Lozano-Durán, A., Bose, S. T., & Moin, P. 2022 Performance of wall-modeled LES with boundary-layer-conforming grids for external aerodynamics. *AIAA J.*, 747–766.

Mauery, T., Alonso, J., Cary, A., Lee, V., Malecki, R., Mavriplis, D., Medic,

G., Schaefer, J., & Slotnick, J. 2021 A guide for aircraft certification by analysis. *Tech. Rep.*, NASA/CR-20210015404.

Meneveau, C., Lund, T., & Moin, P. 1992 Search for subgrid scale parameterization by projection pursuit regression. *Proceedings of the Summer Program*, Center for Turbulence Research, Stanford University, pp. 61–81.

Moin, P., Squires, K., Cabot, W. & Lee, S. 1991 A dynamic subgrid-scale model for compressible turbulence and scalar transport. *Phys. Fluids A*, 2746–2757.

Park, M. A., Alauzet, F., & Michal, T. 2023 HLPW-4/GMGW-3: Mesh adaptation for RANS technology focus group workshop summary. *J. Aircraft*, pp. 1–19.

Poinsot, T. J. & Lele, S. K. 1992 Boundary conditions for direct simulations of compressible viscous flows. *J. Comput. Phys.* **101**, 104–129.

Rumsey, C. L., Slotnick, J. P. & Sclafani, A. J. 2019 Overview and summary of the third AIAA High Lift Prediction Workshop. *J. Aircraft*, 621–644.

Whitmore, M. P., Griffin, K. P., Bose, S. T., & Moin, P. 2021 Large-eddy simulation of a Gaussian bump with slip-wall boundary conditions. *Annual Research Briefs*, Center for Turbulence Research, Stanford University, pp. 45–58.